Orbit Determination Uncertainty Distributions and Mappings in an Unstable Halo Orbit

D. J. Scheeres,[1] D. Han,[2] and Y. Hou[3]

The dynamics of orbit uncertainty in an unstable orbital environment are discussed with specific application to the orbit determination of a halo orbit about the Earth–Sun L1 point. This article documents a simplified orbit determination covariance program developed under Telecommunications and Mission Operations Division Technology support. The program is ideally suited to investigate spacecraft trajectory navigation in challenging environments, where the basic dynamics of the trajectory can no longer be modeled using near-Keplerian motion. The model incorporates a range of dynamical models including the restricted three-body problem, the attendant square-root information (SRIF) and state transition matrix integrations, stochastic acceleration effects on the SRIF matrix, and a simplified yet qualitatively accurate model of Doppler data. A series of computations is performed showcasing the program's ability to analyze the dynamics of orbit uncertainty distribution in unstable orbital environments.

I. Introduction

The dynamics of orbit determination uncertainties are studied for a spacecraft in an unstable halo orbit in the Earth–Sun system. To bring the essential nature of the dynamics into clear focus, we use simple, yet qualitatively accurate, models for the spacecraft dynamics and for the orbit determination measurements. The orbit trajectory is analyzed using the Hill problem, which has a very simple specification yet contains all the essential difficulties of the more general restricted three-body problem [1]. The measurement information content is modeled using the classic Hamilton–Melbourne analysis [2], modified so that it can be used in a square-root information filter formulation. Finally, for realism, our model includes process noise in the form of stochastic accelerations that modify the dynamics of the orbit uncertainty. The current model does not address the non-linear effects that an unstable manifold will have on the orbit uncertainty distribution, but leaves this for future investigations (cf. Junkins et al. [3] for an introduction to this problem for near-Keplerian orbits).

The situation studied with the model investigates the basic processes at work in the orbit determination of a spacecraft in a highly unstable libration point halo orbit [4]. This is a fundamentally different orbital

[1] Department of Aerospace Engineering, The University of Michigan, Ann Arbor.

[2] Navigation and Flight Mechanics Section.

[3] Graduate Student, Department of Aerospace Engineering and Engineering Mechanics, Iowa State University, Ames.

The research described in this publication was carried out by the Jet Propulsion Laboratory, California Institute of Technology, under a contract with the National Aeronautics and Space Administration.

environment from that found for planetary or solar orbiters, as evidenced by recent results concerning the design and implementation of the Genesis mission [5], where extremely sensitive trajectories must be flown in an environment where there are great pressures to decrease the total tracking time of spacecraft (in order to decrease overall costs). Using the research model specified in this article is a first step to an improved understanding of orbit determination in such unstable orbital environments. By properly understanding these situations, it becomes possible to understand the impact of reduced tracking on uncertainty distributions, and may eventually lead to the identification of "optimal" times to track the spacecraft—potentially leading to reduced tracking times during other periods.

II. Model Definition

A. Force Model and Trajectory

This article models a spacecraft trajectory that mimics the Genesis halo orbit, a highly unstable, non-Keplerian trajectory [5]. To define the trajectory, we use an approximation to the three-body problem, known as Hill's problem [1], to model the spacecraft motion. This approximate model is simple to state yet fully captures the relevant dynamics of the three-body problem for motion close to the second, smaller primary (Earth in this case). There are three basic assumptions needed to derive this model [6], all satisfied for the Earth–Sun system: that the spacecraft is relatively close to the Earth, that the mass of the Earth is much smaller than that of the Sun, and that the Earth lies on a near-circular orbit about the Sun. Making these assumptions leads to the equations of motion, specified in the frame centered at the Earth and rotating with the Earth–Sun line:

$$\left.\begin{aligned} \ddot{x} - 2\omega\dot{y} &= \frac{\partial V}{\partial x} \\ \ddot{y} + 2\omega\dot{x} &= \frac{\partial V}{\partial y} \\ \ddot{z} &= \frac{\partial V}{\partial z} \end{aligned}\right\} \tag{1}$$

$$V = \frac{\mu}{r} + \frac{3}{2}\omega^2 x^2 - \frac{1}{2}\omega^2 z^2 \tag{2}$$

where $r = \sqrt{x^2 + y^2 + z^2}$, ω is the Earth's rotation frequency about the Sun (corresponding to a period of one year) and is the rotation rate of the coordinate frame, and μ is the mass parameter of the Earth. In this rotating frame, the x-axis points away from the Sun and the z-axis points normal to the Earth's orbital plane, the y-axis completing the triad. These equations of motion contain analogues to the L1 and L2 points in the three-body problem and can recreate all the qualitative dynamical phenomena about these points [7]. It should be noted that any dynamical model can be used in place of the above one. We focus on this model for definiteness in this article.

The equations in Eq. (1) have been numerically integrated to find a periodic halo orbit with characteristics similar to the Genesis halo orbit. The orbit has a period of just under 179 days and is plotted (in the coordinate frame rotating with the Sun–Earth line) in Figs. 1 through 3. This is an unstable periodic orbit, with a single hyperbolic instability. The Lyapunov characteristic exponent (LCE) of the orbit corresponding to the hyperbolic instability is 4.756×10^{-7}/second, or 0.041/day, corresponding to an expansion of 1.562×10^3 over one orbit period. Corresponding to the hyperbolic unstable term is a hyperbolic stable term with an LCE equal and negative to the unstable LCE, corresponding to a contraction of 6.4×10^{-4} over one orbit period. The remaining terms consist of a two-dimensional center manifold

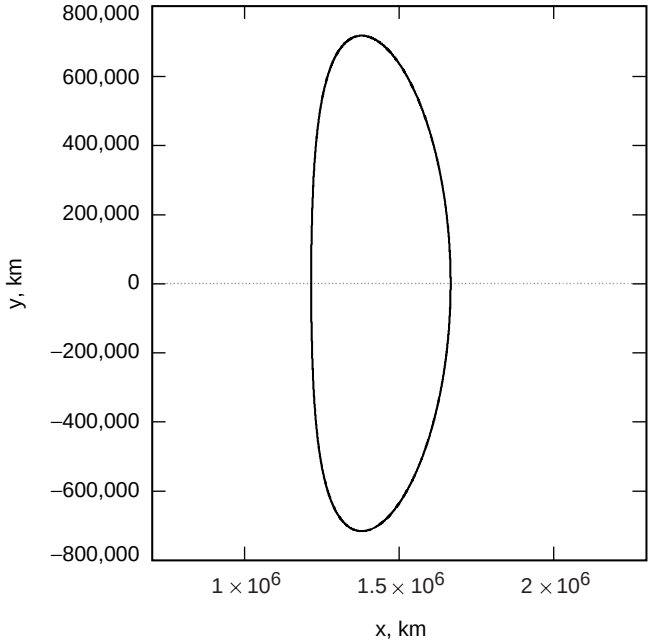

Fig. 1. An x–y projection of a halo orbit. The Sun lies along the +x-direction, and the Earth lies along the –x-direction. Motion occurs in the counterclockwise direction.

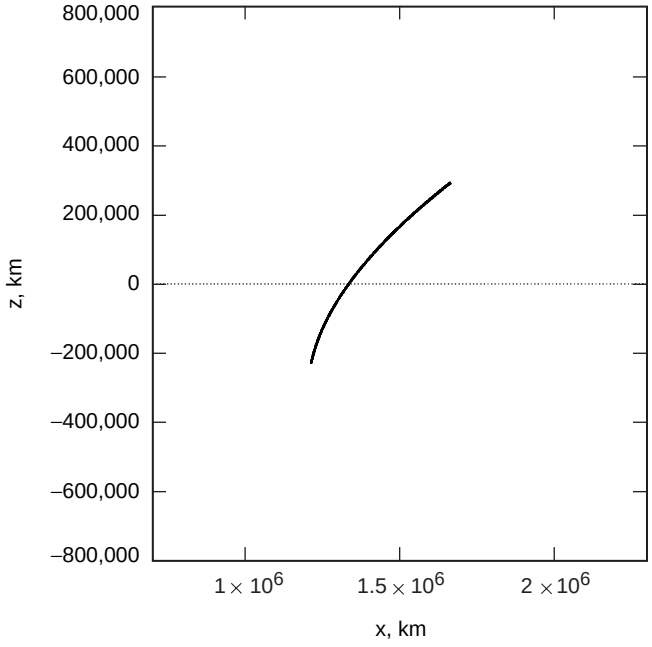

Fig. 2. An x–z projection of a halo orbit. The Sun lies along the +x-direction, and the Earth lies along the –x-direction. Due to symmetries in the model, the periodic motion projects onto a line in this coordinate plane.

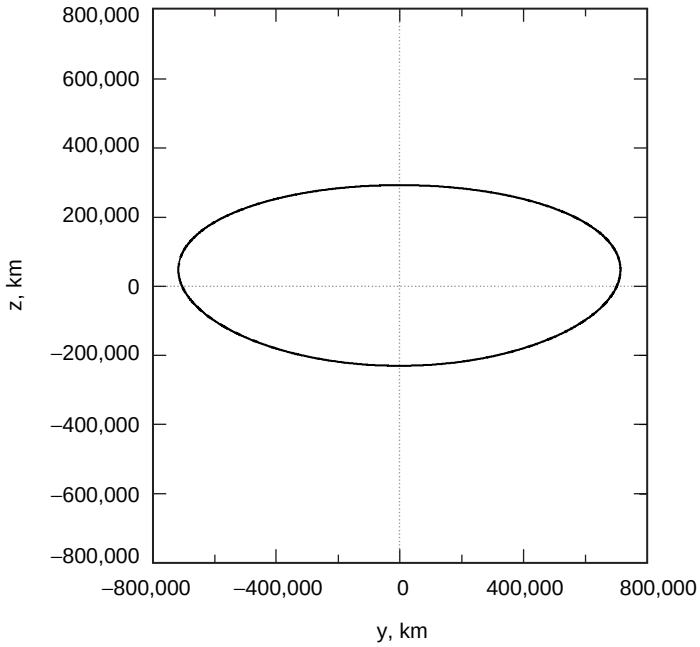

Fig. 3. A y–z projection of a halo orbit. Motion occurs in the counterclockwise direction.

with an oscillation period slightly greater than the orbit period, plus the usual two unity eigenvalues for a closed periodic orbit corresponding to displacements along the orbit and along the surface of constant Jacobi energy [8].

B. Trajectory Stability Characterization

For the analysis performed here, it is the stability properties of the trajectory over times less than one orbit period that are important. For the orbit determination process, we are interested in the orbital dynamics between measurement updates, which occur every few days to weeks. To accommodate this, a generalization of the concept of stable and unstable orbits must be made that applies to relatively short periods of time, what we call the local stability characteristics of the orbit.

These characteristics can be defined using the state transition matrix (STM) evaluated along the trajectory. The STM, $\Phi(t, t_o)$, is computed by integrating the variational equations simultaneously with the trajectory equations:

$$\dot{\Phi}(t, t_o) = A\Phi(t, t_o) \tag{3}$$

$$\Phi(t_o, t_o) = I_{6\times 6} \tag{4}$$

$$A = \begin{bmatrix} 0_{3\times 3} & I_{3\times 3} \\ V_{rr} & 2\omega J \end{bmatrix} \tag{5}$$

$$J = \begin{bmatrix} 0 & 1 & 0 \\ -1 & 0 & 0 \\ 0 & 0 & 0 \end{bmatrix} \tag{6}$$

where V_{rr} is the second partial of the force potential V with respect to the spacecraft position vector. The matrix A will vary with the position of the spacecraft in its halo orbit. Thus, the STM is implicitly a function of the current and initial time as well as the initial state, or $\Phi(t, t_o; \mathbf{r}_o, \mathbf{v}_o)$. Thus, when the computation of the STM is initialized at different locations along the orbit, its local characteristics are expected to change. It is only when the STM is computed over one (or multiple) orbit periods that it is equal to the monodromy map [8] and the stability characteristics become independent of initial time and state, according to Floquet Theory [9].

Now consider the general situation when the STM maps between two times within the nominal periodic orbit, $\Phi(t, t_o; \mathbf{r}_o, \mathbf{v}_o)$, where $t - t_o$ is less than one orbit period. The eigenvalues and eigenvectors of Φ can be computed at each moment of time and are designated as $(\lambda_i, \mathbf{e}_i, \mathbf{f}_i), i = 1, 2, \cdots, 6$, where the λ_i are the eigenvalues of Φ, the $\mathbf{e}_i$ are the corresponding right eigenvectors of Φ, and the $\mathbf{f}_i$ are the corresponding left eigenvectors of Φ. The state transition matrix can then be expressed as [10]

$$\Phi = \sum_{i=1}^{6} \lambda_i \mathbf{e}_i \mathbf{f}_i^T \tag{7}$$

The eigenvalues λ_i follow the same basic rules as are found for periodic orbits [8], where if λ_i is an eigenvalue then so are $\bar{\lambda}_i$, λ_i^{-1}, and $\bar{\lambda}_i^{-1}$, where the overbar denotes complex conjugation.

For a given Φ, we consider an eigenvalue with $|\lambda_i| > 1$ to be unstable, and its corresponding right eigenvector $\mathbf{e}_i$ to define its local "unstable manifold," i.e., the direction relative to the nominal trajectory in which the instability acts. An eigenvalue with $|\lambda_i| < 1$ is considered to be stable, and its corresponding right eigenvector $\mathbf{e}_i$ defines its local "stable manifold." Finally, the eigenvalues with $|\lambda_i| = 1$ are oscillatory, and their eigenvectors define the center manifold. Whereas the STM computed over one period about a periodic orbit in a time-invariant system will always have two eigenvalues equal to 1, an STM computed over a time span non-commensurate with the orbital period will, in general, not have any eigenvalues equal to unity. Rather, the unity eigenvalues for the monodromy map will in general lie on the unit circle, but off of the real axis, when evaluated over less than one period.

As defined above, the local manifolds ($\mathbf{e}_i$) and characteristics (λ_i) of the orbit are a function of time and initial state on the periodic orbit. As the time is varied for a given initial state, the spectrum of the STM can suffer bifurcations and collisions, similar to the possible changes in the stability of a periodic orbit as the problem parameters are varied [8]. As an example, we show the eigenvalues of our periodic orbit as a function of time in Fig. 4. To "normalize" our presentation of eigenvalues, the plot shows the finite-time Lyapunov characteristic exponents (LCEs) [11], defined as

$$\text{LCE}_i = \frac{\ln |\lambda(t, t_o)_i|}{t - t_o} \tag{8}$$

where $|\lambda(t, t_o)_i|$ is the magnitude of the ith eigenvalue of the STM at time t, and $t - t_o$ is the length of time from the start of the STM mapping to the current time. We note that the hyperbolic roots (those with strongly positive and negative LCE values) remain defined as a function of time, but that the oscillatory roots (those with zero LCE values) experience short intervals in time when they bifurcate into hyperbolic and complex roots, and back to oscillatory roots. As expected, the LCEs approach the computed stability characteristics of the periodic orbit as time increases, and, if evaluated after multiples of the orbit period ($\sim$179 days), we find that the LCEs are equal to the periodic orbit's characteristics as computed from the monodromy map. It must be noted that the particular form of the spectrum shown in Fig. 4 is peculiar to our specific periodic orbit. If a significantly different periodic or non-periodic orbit were evaluated, the resulting LCEs could have a significantly different time signature.

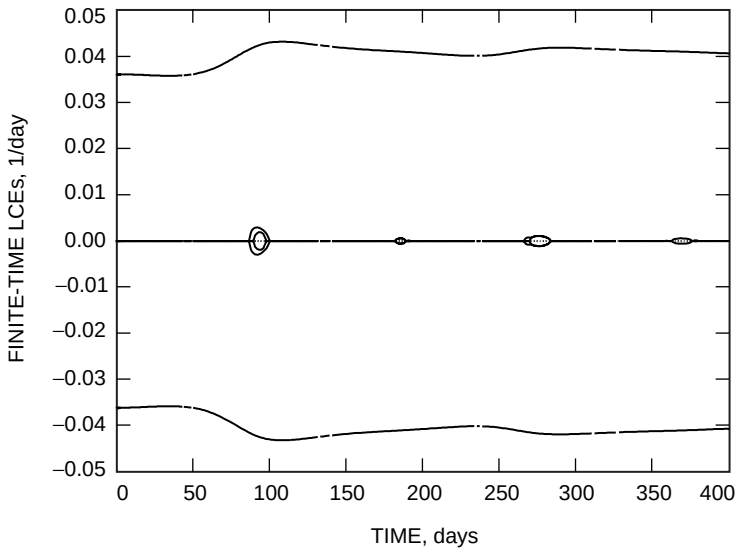

Fig. 4. Finite-time LCEs for a mapped STM along the periodic orbit as a function of time. Note the dominant stable and unstable LCEs and that the center manifold LCEs become hyperbolic and complex over limited intervals of time.

Figure 4 corresponds to the pure mapping of an orbit forward in time, but does not represent the situation once measurements are incorporated into the dynamical system. In this case, the orbit uncertainty distribution becomes updated "impulsively" after every measurement and the STM must be re-mapped, starting from the identity matrix. To give an example of how such updates modify the trajectory characteristics, we plot the dominant unstable hyperbolic LCE of the orbit with periodic resets of the STM back to the identity matrix. This corresponds to the orbit covariance being re-normalized after every measurement opportunity and the distribution of orbit uncertainty being updated. In the presence of these updates, we see a clear pattern emerge for the variation of the LCEs as a function of time, shown in Fig. 5. Thus we see that the properties of the unstable manifold, as they pertain to the mapping of the orbit uncertainty, will change as a function of frequency of measurement. As the updates to the STM become near continuous, the LCEs approach the spectrum of the A matrix in Eq. (5) evaluated along the periodic orbit [12].

C. Filter Model

For accuracy and convenience purposes, the orbit uncertainties are computed and mapped using the square-root information filter (SRIF) formulation [13]. To define the SRIF matrix, first recall the relation between the orbit covariance and information matrix (c.f. Battin [14]):

$$P(t, t_o) = \Lambda(t, t_o)^{-1} \tag{9}$$

where P is the orbit covariance matrix and Λ is the orbit information matrix. The SRIF matrix is then found by computing the square root of the information matrix, defined via

$$\Lambda = R^T R \tag{10}$$

where R is defined as the SRIF matrix. To propagate the orbit uncertainty (or information), we propagate the SRIF matrix R due to its improved numerical properties. In the absence of measurements and stochastic accelerations, the SRIF matrix is the adjoint to the STM matrix and maps as

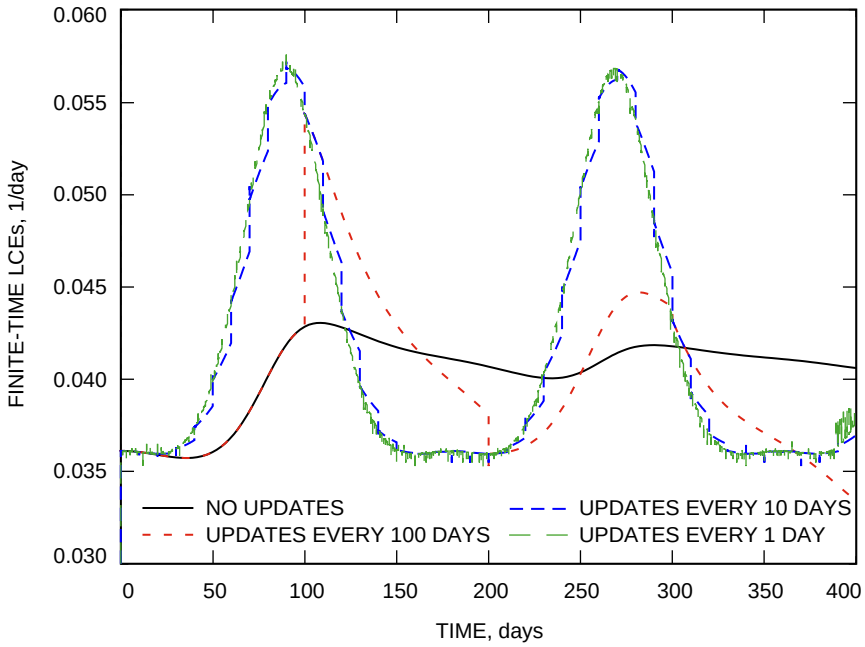

Fig. 5. Maximum finite-time LCEs for mapped STMs updated at different frequencies, showing that the character of the local unstable manifold will change as a function of orbit geometry and tracking.

$$R(t, t_o) = R(t_o)\Phi(t_o, t) \tag{11}$$

The presence of stochastic accelerations destroys this ideal property, and the SRIF matrix is governed by the following differential equation:[4]

$$\dot{R} = -RA - \frac{1}{2}RBP_\omega B^T R^T R \tag{12}$$

where A is the same matrix as defined in Eq. (5) for the variational equations (the partial of the non-linear state dynamics with respect to the current state), P_ω represents the covariance of the process noise (i.e., random acceleration inputs) and is assumed to be constant, and B maps this noise into the dynamics.

In the current model, the stochastic accelerations are treated as having a constant steady-state uncertainty, implying that they are not being estimated by the orbit determination filter. Under this assumption, the matrix B maps P_ω only into the velocity space of the SRIF matrix, and the covariance matrix P_ω has the form

$$P_\omega = 2\tau\sigma_a^2 I_{3\times 3} \tag{13}$$

where τ is the correlation time of the stochastic accelerations and σ_a is the steady-state uncertainty of the acceleration.

[4] D. J. Scheeres, "Derivation of a Generalized Form of the SRIF Differential Equation," JPL Interoffice Memorandum 314-564 (internal document), Jet Propulsion Laboratory, Pasadena, California, 1993.

Given these definitions, it is possible to directly integrate the orbit uncertainty dynamics in time as the orbit trajectory and state transition matrix are integrated forward in time. The steady-state stochastic acceleration and its correlation time are now parameter inputs to our dynamical system.

D. Measurement Models

Finally, measurements are incorporated into our system to develop a realistic model of orbit determination uncertainty. We assume the usual radio metric measurements of Doppler data. As this is not a precision simulation, but a qualitative simulation, it is not necessary to model the Doppler data with high precision. Rather, we need a formulation that correctly incorporates the main contribution of these measurements into the orbit information matrix.

To incorporate the Doppler data measurement, we revisit the classic analysis of the information content from a single pass of Doppler data performed by Hamilton and Melbourne [2]. This analysis shows that the main information extracted from a Doppler pass is the location of the spacecraft in the plane-of-sky and the line-of-sight velocity of the spacecraft with respect to the Earth. If the orbit uncertainty dynamics are properly mapped between measurement passes, and the basic measurement information is incorporated into the SRIF matrix at each pass, we can realistically model the evolution of orbit uncertainty over time.

To first order, the Doppler signal from a spacecraft is only a function of its radial speed (relative to the station), its declination above the Earth's equator, and its right ascension as measured relative to the tracking station. If we denote these three variables as a vector $Y = [\dot{r}, \delta, \alpha]$, where $\dot{r}$ is the radial rate, δ the spacecraft declination, and α its right ascension, and if we designate the Doppler measurement by $\dot{\rho}$, then the information content of a single tracking pass can be formulated as [15]

$$\Delta\Lambda = \frac{1}{\sigma_{\dot{\rho}}^2 T} \int_{-T/2}^{T/2} \left(\frac{\partial \dot{\rho}}{\partial Y}\right)^T \left(\frac{\partial \dot{\rho}}{\partial Y}\right) dt \tag{14}$$

where T is the total tracking pass length and $\sigma_{\dot{\rho}}$ is the noise of the Doppler measurement. Carrying out the operations and integration yields

$$\Delta\Lambda = \frac{1}{\omega \sigma_{\dot{\rho}}^2 \Delta t} \begin{bmatrix} 2\psi & 0 & -2B\sin\psi \\ 0 & \frac{A^2}{2}\big(2\psi - \sin(2\psi)\big) & 0 \\ -2B\sin\psi & 0 & \frac{B^2}{2}\big(2\psi + \sin(2\psi)\big) \end{bmatrix} \tag{15}$$

$$A = R_s \omega \sin\delta \tag{16}$$

$$B = R_s \omega \cos\delta \tag{17}$$

where R_s is the tracking station distance from the Earth's spin axis, δ is the spacecraft declination in the Earth frame, ω is the Earth's rotation rate, ψ is the half-angle of the tracking pass, $\sigma_{\dot{\rho}}$ is the Doppler measurement noise, and Δt is the time interval over which the noise value is defined. We assume that the Doppler tracking data have an accuracy $\sigma_{\dot{\rho}} \sim 0.1$ mm/s for $\Delta t = 60$ s.

For a SRIF filter, the inclusion of measurements is usually performed using Householder transformations [13] to update the SRIF matrix with the measurement partials, properly scaled to represent the data noise. Generally, Doppler measurements are scalar measurements, and the measurement partial is

a simple row vector. However, in our approach we combine the entire Doppler pass into one coupled measurement of the three quantities of range rate, declination, and right ascension. Since these quantities are integrated over a pass of Doppler data, there is not a convenient description of them outside of the information matrix. To incorporate these measurements into the SRIF matrix, the measurement partial of these quantities must be computed, which in this case will be a matrix that the Householder transformation can accommodate.

To derive this effective measurement partial, we note that the information matrix of a single Doppler pass can, itself, be expressed as a square-root matrix:

$$\Delta\Lambda = (\Delta R)^T \Delta R \tag{18}$$

Applying a square-root algorithm to the 3-by-3 matrix yields

$$\Delta R = \frac{1}{\sqrt{\omega\sigma_{\dot{\rho}}^2 \Delta t}} \begin{bmatrix} \sqrt{2\psi} & 0 & \dfrac{-2B\sin\psi}{\sqrt{2\psi}} \\ 0 & \dfrac{A}{\sqrt{2}}\sqrt{2\psi - \sin(2\psi)} & 0 \\ 0 & 0 & B\sqrt{\psi + \sin(2\psi)/2 - 2\sin^2(\psi)/\psi} \end{bmatrix} \tag{19}$$

The general procedure for updating the spacecraft SRIF matrix given our measurement partial ΔR is to choose a Householder transformation T_H such that [13]

$$T_H \begin{bmatrix} R \\ \Delta R \end{bmatrix} = \begin{bmatrix} R' \\ 0 \end{bmatrix} \tag{20}$$

where R' is the new, updated SRIF matrix, which is then propagated forward in time.

With the current assumptions, the information content of an entire Doppler measurement pass can be combined with the a priori information using purely analytical models. The use of such a simple model provides flexibility in simulating the effect of different tracking schedules and geometries, while not requiring that a detailed tracking schedule be implemented. To properly model the information content of the Doppler data, a transformation from the Earth equatorial coordinate frame to the Earth ecliptic frame (which is the frame that the spacecraft orbit is specified in) must be provided as well. This transformation introduces an additional free parameter into our analysis, which we formulate as a phase angle, but which really corresponds to the solar day at the start of the simulation. By varying this phase angle, we vary the declination of the spacecraft over the time period in question. In general, this will also cause the results of our orbit determination simulation to vary. Figure 6 shows declination histories of the trajectory depending on the initial phase angle.

E. Validation of the Model

In order to validate our simplified model of orbit determination mapping and uncertainty, a comparison of the overall results of our model was made with precision orbit determination studies performed for the Discovery mission Genesis.[5] Comparisons between our simplified model and the precision models at JPL yielded covariance agreements to an acceptable level, indicating that the simplified model captures

[5] D. Han, E. Carranza, B. G. Williams, and D. J. Scheeres, "Navigation Study Results for Genesis Mission," JPL Interoffice Memorandum 312.A-97-016 (internal document), Jet Propulsion Laboratory, Pasadena, California, July 15, 1997.

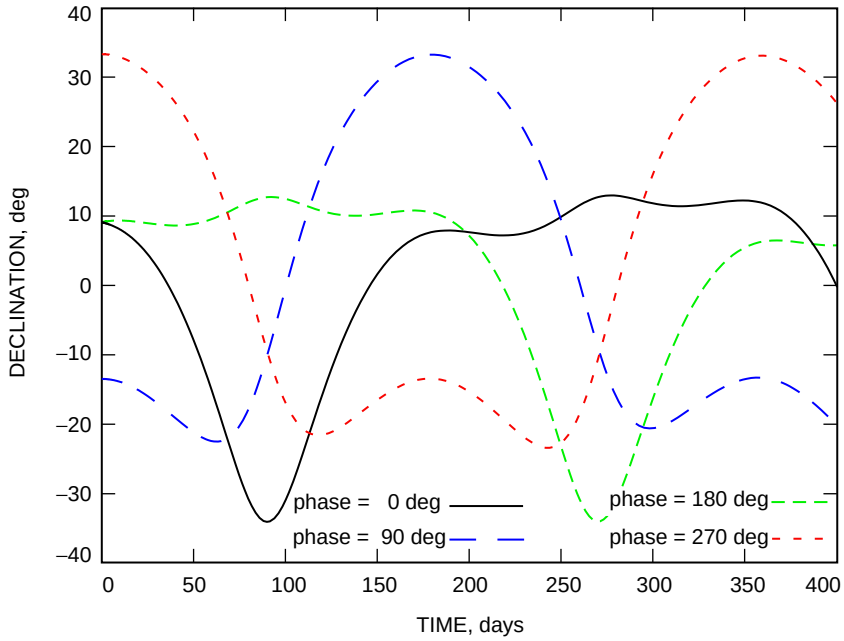

Fig. 6. Spacecraft declination angles for different initial phase angles. A 0-deg phase at epoch corresponds to the fall equinox, a 90-deg phase to the winter solstice, a 180-deg phase to the spring equinox, and a 270-deg phase to the summer solstice.

the basic processes at work in this situation. Detailed comparisons between the results does not make sense since the Genesis study was made using high-precision force and measurement models and a non-repeating trajectory. The model described above has been carefully formulated to minimize inputs while retaining a realistic model of the orbit determination function. This design allows the model to be used for basic research into spacecraft navigation and orbit determination without having to specify detailed parameters. Also, the simple design allows for the entire model to be contained within a single program, eliminating the need for file transfers between the different functions of the model.

III. Orbit Uncertainty Dynamics

Having defined our model problem of an unstable orbit and the accumulation and mapping of information along that orbit, we carry out a number of simple computations to better quantify and understand the influence of the unstable orbit on the orbit information and uncertainty distribution. All our numerical calculations presented assume an initial phase angle of 270 deg; the resulting declination history can be found in Fig. 6. The latitude of the Doppler tracking station is assumed to be 30 deg and the pass angle to be 30 deg.

In the discussions, we will use the direction of the local unstable manifold and the direction of the maximum orbit uncertainty in order to establish our results. As defined in Section II, the local unstable manifold for our trajectory is computed from the state transition matrix and corresponds to the eigenvector of the largest eigenvalue with magnitude greater than one. From Figs. 4 and 5 it is clear that this largest eigenvalue is unambiguously defined for the orbit under consideration. The direction of maximum orbit uncertainty is defined using the orbit covariance matrix. At each time step, we compute the eigenvalues and eigenvectors of the covariance matrix and find the maximum eigenvalue of the matrix. The direction of maximum uncertainty is then defined by the eigenvector associated with the maximum eigenvalue. The influence of the local unstable manifolds on the orbit uncertainty distribution can then be gauged by comparing the relative directions of the unstable manifold and the maximum uncertainty. In the following, this comparison is made by taking the dot product of these two directions, where, since the

eigenvectors of these matrices are six-dimensional, the dot product is taken between two six-dimensional vectors. When this projection is close to or equal to one, the unstable manifold can be considered to be exerting a strong influence on the orbit uncertainty distribution. When the projection is close to or equal to zero, the unstable manifold can be considered to be "well-determined," indicating that the sensitivity of trajectories along this direction is aiding in its determination. If the unstable manifold and the maximum uncertainty direction were uncorrelated with each other, the average projection of these directions would lie in the range of 0.4 to 0.6.

A. Overall Orbit Determination Performance

Using our base trajectory, we computed the orbit determination uncertainty of the spacecraft over two halo orbit periods. Doppler passes are included every 2 or 25 days, and the trajectories have a steady-state stochastic acceleration of 10^{-16}, 10^{-12}, or 10^{-10} km/s^2 with correlation times of approximately 1/2 day. Presented in Figs. 7 and 8 are plots of the average position and velocity uncertainties as functions of time. The average was computed by taking the trace of the appropriate sub-matrix of the covariance, dividing by three, and taking the square root. This gives us an overall measure of the orbit quality. It also confirms the steady-state expectations of the system.

B. Mapping of Orbit Determination Uncertainties Without Measurements

To show that the direction of largest uncertainty no longer lies in the down-track direction, the maximum uncertainty direction and local unstable manifold were projected onto the down-track direction of the orbit. Were the down-track direction still the dominant direction, we would expect the maximum uncertainty direction to approach a projection value of 1 with the down-track direction. The results of this computation are shown in Fig. 9. This figure corresponds to a mapping of an initial orbit uncertainty distribution with no measurement updates. What is clear from this figure is that the unstable manifold and the maximum uncertainty directions approach each other, and that the maximum uncertainty direction does not align itself with the down track.

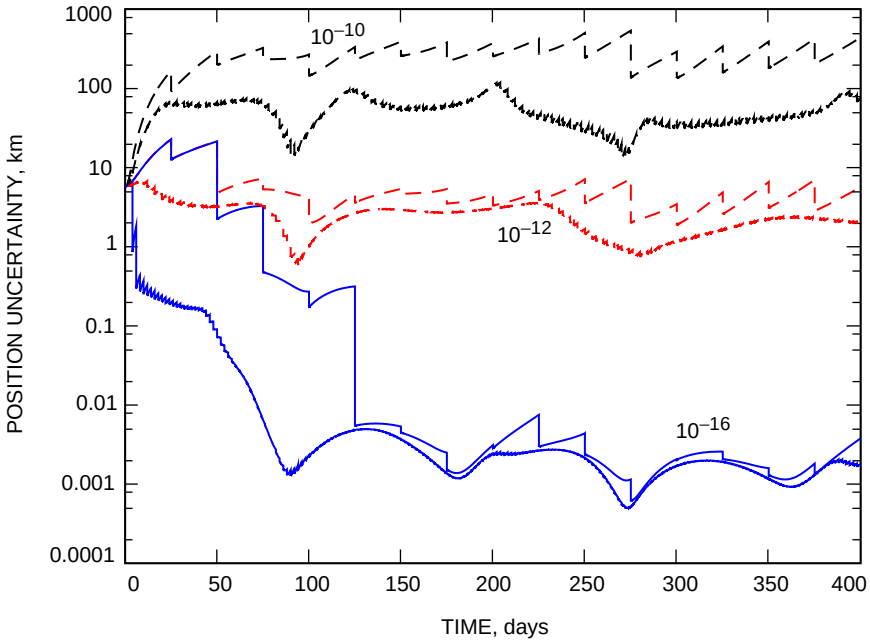

Fig. 7. Average position covariance for different stochastic acceleration levels and tracking schedules of every 2 days (smoother lines) and 25 days (saw-toothed lines).

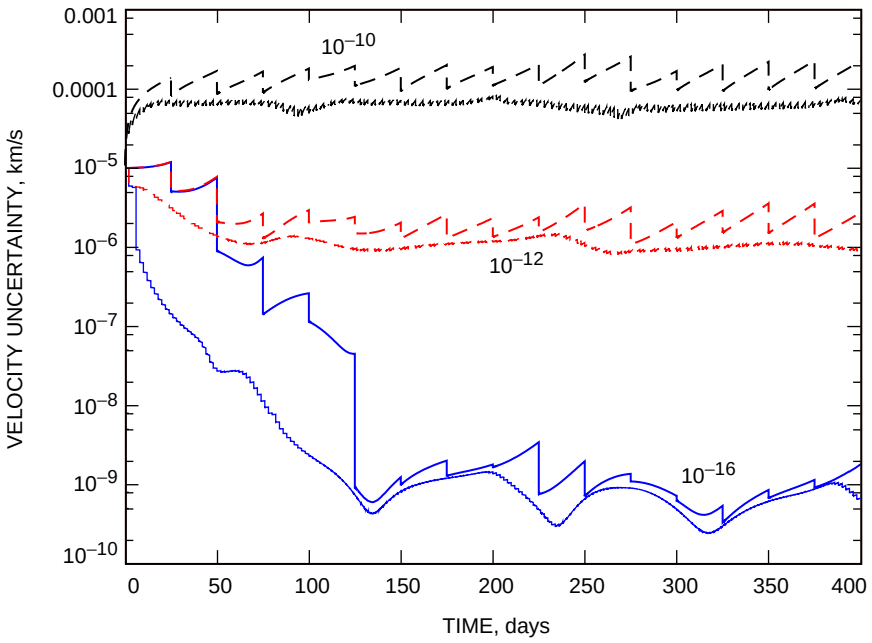

Fig. 8. Average velocity covariance for different stochastic acceleration levels and tracking schedules of every 2 days (smoother lines) and 25 days (saw-toothed lines).

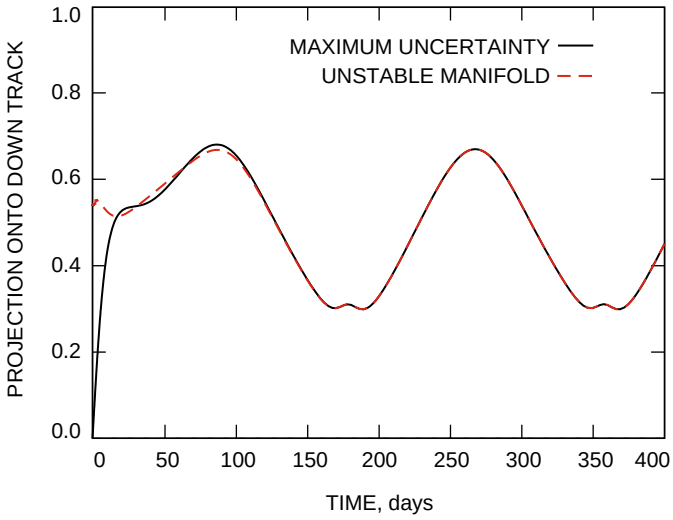

Fig. 9. The unstable manifold and maximum direction of uncertainty projected onto the down-track direction for a mapped uncertainty distribution with no measurements.

To show this more clearly, we plot the projection of the maximum uncertainty direction onto the local unstable manifold in Fig. 10. As the projection approaches a value of unity, this clearly indicates that the unstable manifold controls the direction of maximum orbit uncertainty. The implication of this is that the direction of largest uncertainty, after mapping for a sufficiently long time period, will not be directly related to the geometry of the orbit but will instead be related to the geometry of the unstable manifold, which is a combination of both position and velocity directions in phase space.

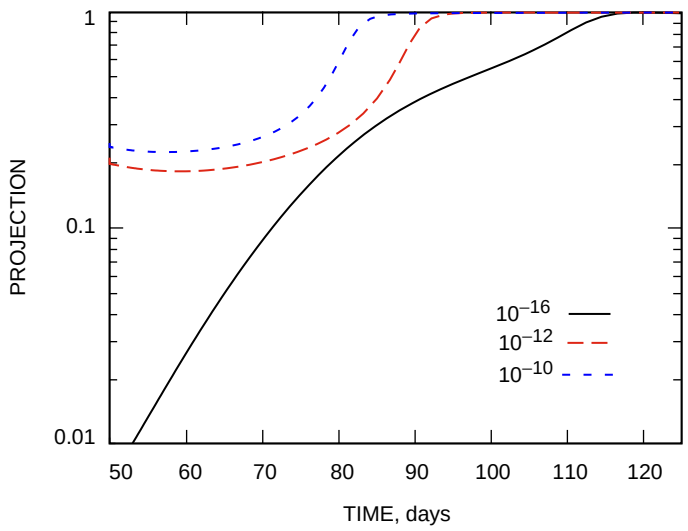

Fig. 10. Projection of the maximum direction of uncertainty along the unstable manifold. The projections are shown after 50 days of tracking with one pass every 2 days. Three different levels of stochastic acceleration are shown.

To bring this effect into sharper focus, we project the maximum orbit uncertainty direction onto the unstable manifold direction and compute the time for the two directions to become aligned with each other. In Table 1 the "entrainment" time for the two directions to come within 10 deg of each other is given as a function of the amount of tracking prior to data cut-off and the level of stochastic acceleration. It is interesting to note that the "average" characteristic time of the orbit is ∼24 days (computed from the periodic orbit's largest characteristic exponent); thus, the orbit uncertainty will grow by an order of magnitude in ∼66 days. This correlates well with the time it takes the orbit uncertainty to become entrained along the unstable manifold. We note some variation in the entrainment time with the level of stochastic accelerations, with the clearest trend being a decrease in time for the larger values of stochastic acceleration. The variation across these parameters is not that significant, however, indicating that the unstable manifold continues to dominate the orbit distribution dynamics even when there are large stochastic accelerations present.

Table 1. Time for the maximum uncertainty direction and the local unstable manifold to align within 10 deg of each other in the absence of tracking. This time varies with the amount of tracking prior to data cut-off and the steady-state level of stochastic accelerations.

Tracking before data cut-off, days	Time to align to within 10 deg		
	Stochastic accelerations,		
	10^{-16} km/s^2	10^{-12} km/s^2	10^{-10} km/s^2
2	68	68	58
50	67	45	41
100	79	62	58
150	89	57	62

C. Effect of Measurements on Orbit Determination Dynamics

Without measurements, the STM directions and maximum covariance uncertainty directions approach each other asymptotically. With measurements, this effect no longer holds, and the direction of maximum uncertainty and the unstable local manifold are no longer simply aligned. In Figs. 11 through 13, we show the projection of the maximum uncertainty direction onto the local unstable manifold, each figure corresponding to a different level of stochastic acceleration and each showing the distributions for a track every 2 and 25 days. Although complicated, there are some basic results that can be extracted from these plots. For the infrequent tracking schedule of one pass every 25 days, there is an obvious trend for the maximum uncertainty direction to align with the unstable manifold—an effect that we characterized in the previous section. Of specific interest, however, is that after the next measurement is incorporated the maximum uncertainty direction becomes more orthogonal to the local unstable manifold. This is direct evidence of the effect discussed earlier, which posited that, with tracking, the unstable manifolds should become better determined in general due to the increased efficiency of measurements along this direction. We see that this effect is pronounced for all levels of stochastic acceleration.

Next we note that the direction of maximum uncertainty tends to be orthogonal to the local unstable manifold—indicated in Figs. 11 through 13 by the projection being relatively small over most of the tracking history. Here, however, there are clear deviations from this effect that should be explained. The same plots generated for different initial phase angles (or initial day of year) exhibit similar spikes in the alignment between the maximum uncertainty direction and the unstable orbit, although their distribution in time is different—indicating that the effect is due to the relative geometry of the spacecraft and measurements. We also note a "smoothing" of the spikes with increasing level of stochastic acceleration. A comprehensive series of comparisons between this projection geometry and other dynamical quantities in the system shows that the strongest correlation with these periods of alignment occurs when the maximum direction of uncertainty is aligned along the direction that is "unsensed" by the Doppler measurements; in position space, this lies along the unit radius vector. Figures 14 through 16 overlay plots of the projection of the maximum uncertainty direction onto the local unstable manifold and into the unsensed direction of the Doppler measurements. The strong correlation between these two indicates that the effect of the increased sensitivity of the unstable manifolds is lost when it is not immediately detectable by the orbit determination measurements. The correlation in Figs. 14 through 16 is strongest for low levels of stochastic acceleration and becomes less strong for larger levels of stochastic acceleration. Periods when this alignment occurs appear to be most closely correlated with periods of slow or swift motion of the spacecraft across the celestial sphere. In either of these cases, apparently, the measurement conditions allow the unstable manifold to be unobservable for an interval of time.

The implications of these effects may be applicable to the design of simplified, robust navigation schemes for single or multiple spacecraft flying in unstable orbital environments. If a consistent prediction of the location and direction of the unstable manifolds can be found for a particular craft, it becomes possible to implement a sensing and control strategy that takes advantage of this effect. A detected growth of uncertainty along this direction could serve as an alert that the orbit determination or control scheme is not performing properly. Conversely, due to the increased efficiency of measurements along this direction, tracking schedules can be designed and optimized to take this into consideration.

IV. Conclusions

This article addresses, at a preliminary level, the linear dynamics of uncertainty distribution, with and without tracking, for a spacecraft in an unstable orbital environment (defined by the presence of positive finite-time Lyapunov characteristic exponents). The numerical results model an orbital situation similar to the proposed Genesis halo orbit trajectory. Interesting results include the divergence of the maximum uncertainty direction and the down-track direction, the relation between the characteristic time of the instability and the time between tracking cessation and dominance of the unstable manifold over the orbit uncertainty distribution, the increased efficiency of measurements along the unstable manifold,

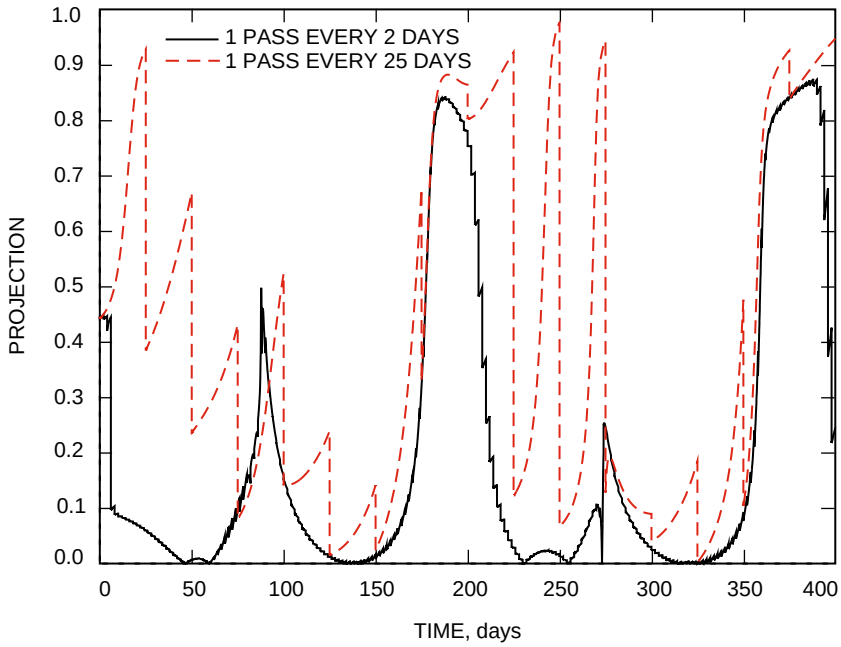

Fig. 11. Projection of the maximum uncertainty direction onto the local unstable manifold for a track every 2 and 25 days with a stochastic acceleration level of 10^{-16} km/s^2.

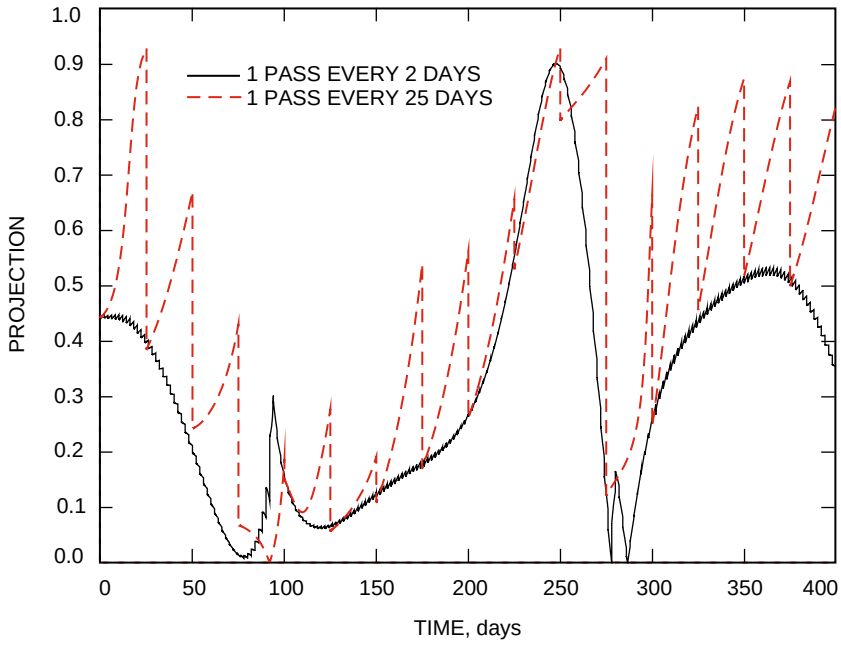

Fig. 12. Projection of the maximum uncertainty direction onto the local unstable manifold for a track every 2 and 25 days with a stochastic acceleration level of 10^{-12} km/s^2.

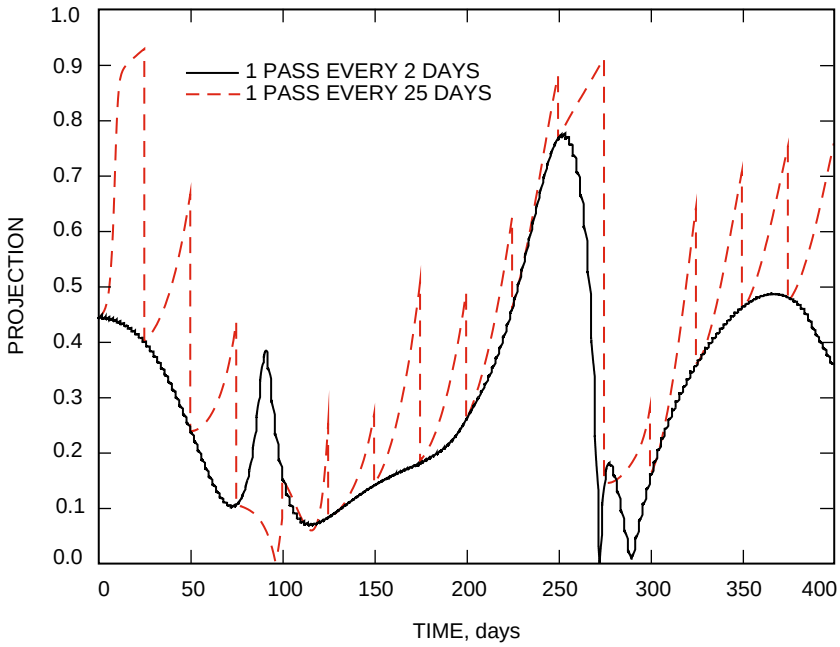

Fig. 13. Projection of the maximum uncertainty direction onto the local unstable manifold for a track every 2 and 25 days with a stochastic acceleration level of 10^{-10} km/s^2.

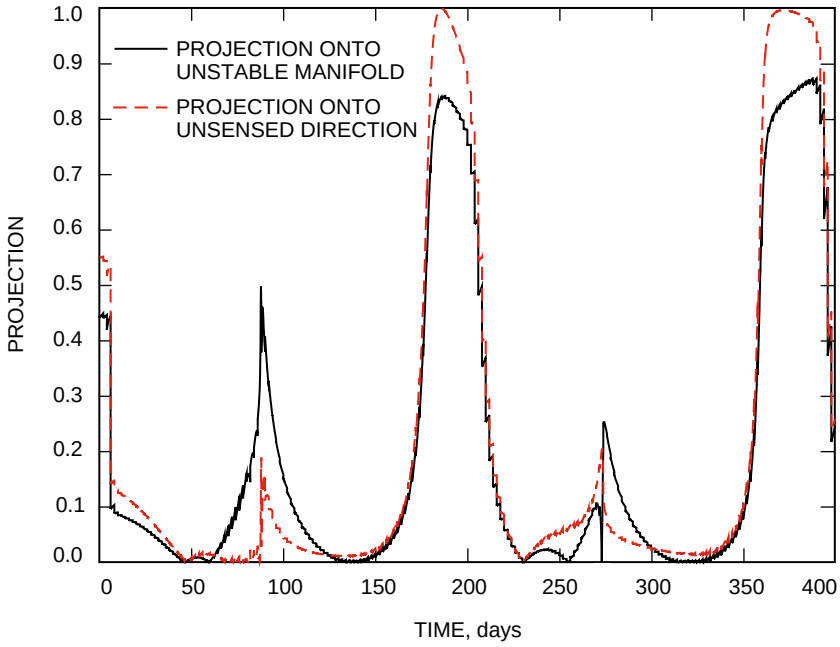

Fig. 14. Projection of the maximum uncertainty direction onto the local unstable manifold and projection of the maximum uncertainty direction onto the "unsensed" direction for a Doppler pass, for the case of one pass every 2 days with a stochastic acceleration level of 10^{-16} km/s^2.

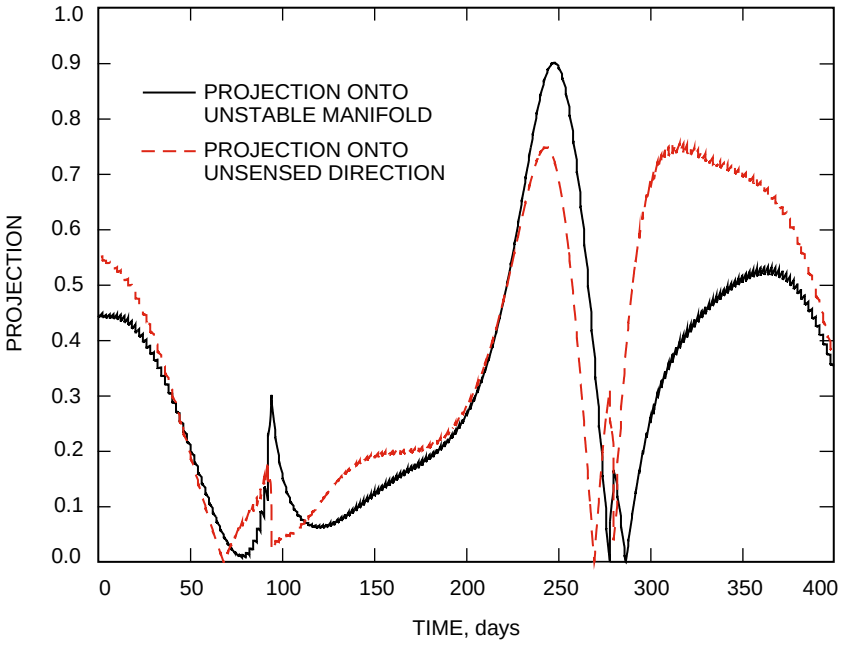

Fig. 15. Projection of the maximum uncertainty direction onto the local unstable manifold and projection of the maximum uncertainty direction onto the "unsensed" direction for a Doppler pass, for the case of one pass every 2 days with a stochastic acceleration level of 10^{-12} km/s^2.

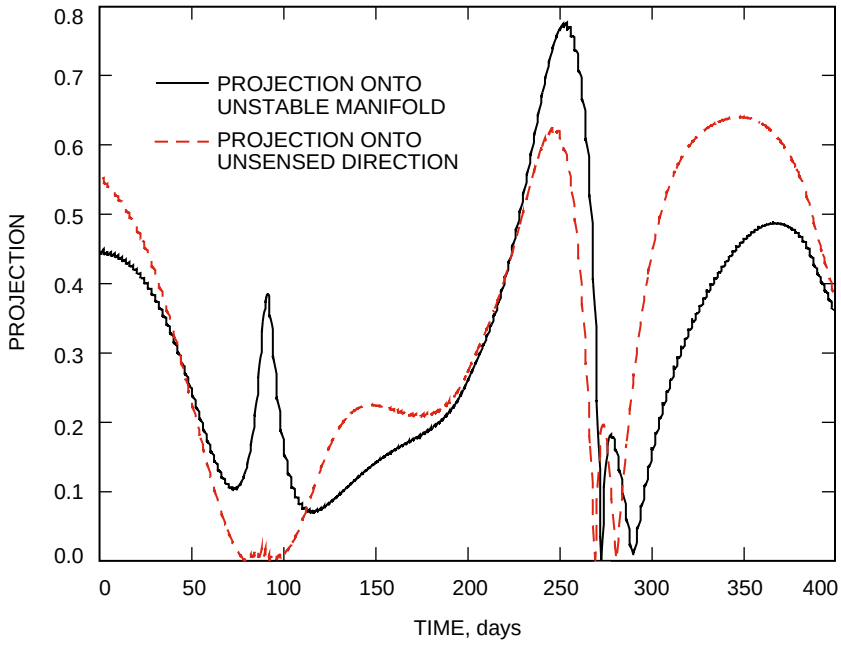

Fig. 16. Projection of the maximum uncertainty direction onto the local unstable manifold and projection of the maximum uncertainty direction onto the "unsensed" direction for a Doppler pass, for the case of one pass every 2 days with a stochastic acceleration level of 10^{-10} km/s^2.

and the tendency of the unstable manifold to be well determined during periods of tracking (when it is observable). These analyses were carried out using a square-root information matrix formulation for numerical robustness, using analytical models of Doppler tracking to account for measurements, and with correlated stochastic accelerations as an input parameter. The models developed in this article will be used in future studies of orbit determination in unstable orbital environments.

References

[1] V. I. Arnold, "Dynamical Systems III," *Encylopedia of Mathematical Sciences*, vol. 3, Berlin: Springer-Verlag, pp. 72–75, 1988.

[2] T. W. Hamilton and W. G. Melbourne, "Information Content of a Single Pass of Doppler Data from a Distant Spacecraft," *Space Programs Summary 37-39*, Jet Propulsion Laboratory, Pasadena, California, vol. III, pp. 18–23, March–April 1966.

[3] J. L. Junkins, M. F. Akella, and K. T. Alfriend, "Non-Gaussian Error Propagation in Orbit Mechanics," *Journal of the Astronautical Sciences*, vol. 44, no. 4, pp. 541–563, 1996.

[4] R. W. Farquhar, *The Utilization of Halo Orbits in Advanced Lunar Operations*, NASA Technical Note D-6365, 1971.

[5] K. C. Howell, B. T. Barden, and M. W. Lo, "Application of Dynamical Systems Theory to Trajectory Design for a Libration Point Mission," *Journal of the Astronautical Sciences*, vol. 45, no. 2, pp. 161–178, 1997.

[6] D. J. Scheeres, "The Restricted Hill Four-Body Problem with Applications to the Earth-Moon-Sun System," *Celestial Mechanics and Dynamical Astronomy*, vol. 70, pp. 75–98, 1998.

[7] A. Wintner, *The Analytical Foundations of Celestial Mechanics*, Princeton, New Jersey: Princeton University Press, pp. 381–382, 1947.

[8] C. Marchal, *The Three-Body Problem*, Amsterdam: Elsevier, pp. 146–158, 1990.

[9] L. Cesari, *Asymptotic Behavior and Stability Problems in Ordinary Differential Equations*, second edition, New York: Academic Press, pp. 55–59, 1963.

[10] J. D. D'Azzo and C. H. Houpis, *Linear Control System Analysis and Design*, second edition, New York: McGraw-Hill, p. 615, 1981.

[11] C. Froeschlé, "The Lyapunov Characteristic Exponents—Applications to Celestial Mechanics," *Celestial Mechanics*, vol. 34, pp. 95–115, 1984.

[12] D. J. Scheeres and N. X. Vinh, "Dynamics and Control of Relative Motion in an Unstable Orbit," AIAA Paper 2000-4135, presented at the Astrodynamics Specialist Conference, Denver, Colorado, August 11–14, 2000.

[13] G. J. Bierman, *Factorization Methods for Discrete Sequential Estimation*, San Diego: Academic Press, 1977.

[14] R. H. Battin, "An Introduction of the Mathematics and Methods of Astrodynamics," *AIAA Education Series*, pp. 661–671, 1987.

[15] S. W. Thurman, "Comparison of Earth-Based Radio Metric Data Strategies for Deep Space Navigation," AIAA-90-2908-CP, 1990.